Chinese Chemical Letters 34 (2023) 108232

Contents lists available at ScienceDirect

Chinese Chemical Letters

journal homepage: www.elsevier.com/locate/cclet

The dispersion of iron nitride among porous carbon fibers to enhance redox conversion for high-performance zinc-iodine batteries

Siyu Ding, Qianwu Chen, Song Chen, Yadong Tian, Jintao Zhang*

Key Laboratory for Colloid and Interface Chemistry, Ministry of Education, School of Chemistry and Chemical Engineering, Shandong University, Ji'nan 250100, China

ARTICLE INFO

Article history:
Received 5 January 2023
Revised 25 January 2023
Accepted 15 February 2023
Available online 19 February 2023

Keywords:
Iron nitride
Porous carbon fibers
Redox conversion
Rechargeable zinc-iodine batteries
Enhanced cycling stability

ABSTRACT

To address the insulating nature and the shuttle effect of iodide species that would deteriorate the battery performance, herein iron nitride is well-dispersed into porous carbon fibers with good flexibility *via* the facile electrospinning method and subsequent pyrolysis. The polyacrylonitrile precursor introduces the nitrogen doping under thermal treatment while the addition of iron acetylacetonate leads to the *in-situ* formation of iron nitride among the carbon matrix. The crucial pyrolysis procedure is adjustable to determine the hierarchical porous structure and final composition of the novel carbon fiber composites. As the self-supporting electrode for loading iodine, the zinc-iodine battery exhibits a large specific capacity of 214 mAh/g and good cycling stability over 1600 h. In the combination of *in-situ*/*ex-situ* experimental measurements with the theoretical analysis, the in-depth understanding of intrinsic interaction between composited support and iodine species elucidates the essential mechanism to promote the redox kinetics of iodine *via* the anchoring effect and electrocatalytic conversion, thus improving cycling life and rate performance. Such fundamental principles on the basic redox conversion of iodine species would evoke the rational design of advanced iodine-based electrodes for improving battery performance.

With the rapid development of science, technology and social progress [1,2], it is urgent to develop novel rechargeable batteries to meet the requirements for energy storage. Rechargeable metal-halogen batteries as promising energy storage devices are attracting much attention [3,4]. With organic electrolytes, alkali metals including lithium [5–8], sodium [9], and others metals are used as anodes to fabricate rechargeable batteries [10,11]. The metal zinc with high theoretical capacity (820 mAh/g) is abundant and relatively inert to air in comparison with other metals [12,13]. Aqueous electrolytes with good ionic conductivity are safer compared to organic systems. Thus, zinc has been coupled with iodine to fabricate rechargeable zinc-iodine batteries [14].

With the increasing attention, it is found that the capacity performance and cycling stability are seriously impeded by the poor conductivity of iodine, the dissolution and shuttle effect of iodine species in electrolyte, resulting in the irreversible capacity fading. Therefore, polymers [15,16], MOFs [17–20], and multidimensional carbon materials are reported as cathode materials to inhibit capacity degradation [21]. Various porous carbon, active carbon fiber (ACF) [22], layered MXene [23,24], graphene [25], CNT and double-layer cathode are reported as the candidate materials to improve the performance of rechargeable zinc-iodine batteries [26,27]. Importantly, the modification of carbon skeleton with metal and/or non-metal elements and compounds can further promote the battery performance [28]. Transition metal oxides, sulfides, nitrides and carbides exhibit electrocatalytic properties for electrocatalysis. Among them, polar iron nitride (Fe_2N) with good electronic conductivity and intrinsic catalytic activity is expert in a wide range of applications. Especially, amorphous Fe_2N structure is crucial to achieve rich defects, that can provide more catalytic sites to promote reaction kinetics [29]. Therefore, it is highly desirable to enhance the iodine adsorption and redox conversion *via* the incorporation with metal carbide or nitride for accelerating electron transfer and improving the reaction kinetics.

As the facile way to produce fibrous materials with controllable diameter and length [15], electrospinning method is combined with the thermal treatment to fabricate three-dimensional porous carbon fiber-based materials. By use of polymers (*e.g.*, PAN, PVP, PVA, PA) as carbon source, the obtained carbon fibers are widely investigated in the energy applications [30]. However, the one-step preparation of metal nitride embedded carbon fibers is rarely reported as conductive support for loading iodine and their underlying interaction mechanism is not clear for fabricating zinc-

* Corresponding author.
E-mail address: jtzhang@sdu.edu.cn (J. Zhang).

https://doi.org/10.1016/j.cclet.2023.108232
1001-8417/

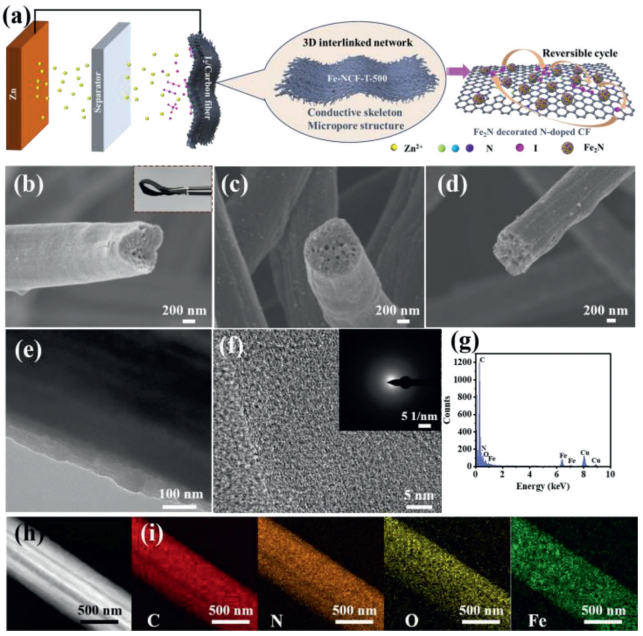

Fig. 1. (a) Schematic illustration for the mechanism of zinc-iodine battery. (b) SEM images of Fe-NCF-700–500, (c) Fe-NCF-800–500, (d) Fe-NCF-900–500. (e, f) TEM images of Fe-NCF-700–500 and SAED pattern. (g) EDS, (h) STEM image, and (i) corresponding elemental mapping images of Fe-NCF-700–500.

iodine battery. Herein, we demonstrated the preparation of iron nitride decorated N-doped carbon fiber as conductive host to immobilize iodine *via* the combination of electrospinning method and carbonization process. With the maximum active material utilization and optimal structural stability, iodine was loaded to fabricate advanced zinc-iodine battery, exhibiting large capacity and improved cycling stability. Combined with the experimental results, the theoretical calculations revealed the chemical interaction between iodine and different substrates along with the physical trapping enhancement to iodine adsorption, thus improving the battery performance. The fundamental study provides basic guidelines to rationally design advanced iodine composite electrode for high-performing zinc-iodine battery.

As shown in Fig. 1a, the obtained Fe_2N decorated porous N-doped carbon fibers with good flexibility can be used as conductive host for loading iodine to fabricate a composite cathode without additional binder to boost iodine conversion. The carbonization temperatures were changed to reveal the influence on iodine redox reactions by regulating the structure and defects of composite electrode. The SEM images (Figs. 1b-d) and TEM images (Fig. S1 in Supporting information) exhibit the highly porous structure of Fe_2N decorated N-doped porous carbon fiber (Fe-NCF) samples due to the decomposition of PS (pore-forming agent) and reconstruction of structure at an elevated temperature. The carbon fibers are intertwined with each other, leading to the formation of electrically conductive framework for rapid mass/charge transfer. The relatively smooth surface of Fe-NCF-700–500 exhibited no nanoparticle was formed during the thermal treatment (Fig. 1e). The similar fiber diameters were obtained under different pyrolysis temperatures (Fig. S1). The Fe-NCF-600–500 exhibits relatively smooth surface (Fig. S2 in Supporting information). However, it is obvious that some small nanoparticles can be obviously seen at the heat treatment above 700 °C (Figs. 1c and d). The carbonization temperature plays a key role in the formation of crystalline particles. High-resolution TEM images of Fe-NCF-800–500 sample verify that the particles are embedded among the fibers (Fig. S4a in Supporting information), showing the lattice fringe of 0.21 nm (Fig. S4b in Supporting information) for the (011) plane of Fe_2N (JCPDS No. 72–2126). The SAED further confirms the presence of crystalline Fe_2N (Fig. S4c in Supporting information). Compared with the Fe-NCF-800–500, the diffraction ring in Fe-NCF-700–500 is not obvious in Fig. 1f, showing the possibility of amorphous structure. This further confirms that temperature affects the formation of Fe_2N nanoparticles, since particles tend to agglomerate at the higher temperature. EDS, STEM and element mapping images display the uniform distribution of C, N, O and Fe elements in Figs. 1g-i.

The iodine can be adsorbed into the porous fiber along with the disappear of yellow color (Fig. 2a), indicating the feasibility of the fiber sample as an iodine-carrying host. The results demonstrate that carbonization temperature affects the structure and morphology of fiber. It has been reported that the ferric nitride can be formed at a low ammonolysis temperature of 500 °C. When temperature raised to 800 and 900 °C, XRD patterns (Fig. 2b) exhibit the diffraction peaks at 40.9° and 42.9° which are ascribed to the (002), (011) planes of Fe_2N (JCPDS No. 72–2126) [31]. However, the SEM images and XRD patterns suggest the amorphous structure of Fe_2N in Fe-NCF-700–500. The existence of amorphous Fe_2N was further verified by Raman spectra. The peaks of the Fe-NCF-700–500 at 200–700 cm^{-1} (Fig. 2c) are ascribed to the iron nitride [32]. Compared with crystalline structures, amorphous structure with uncoordinated atoms and defect structures would provide more active sites for electrocatalytic processes. The presence of Fe_2N on carbon fibers would improve the interaction of the host with iodine species to promote the conversion reversibility among iodine species. Moreover, by introducing nitrogen defects into carbon skeleton, the electronic structure of the material can be regulated so that the ability of electron transfer can be improved [33].

With the uniform distribution of nitrogen and iron (Fig. S5a in Supporting information) on the fiber, the successful loading of active iodine was also observed. However, the corresponding XRD pattern (Fig. S5b in Supporting information) does exhibit the absence of crystalline iodine. For Raman spectrum in Fig. 2d, the I_D/I_G value of Fe-NCF decreases from 1.46, 1.31, to 1.04 with the increase of temperature, suggesting the reduction in the degree of carbon defect [34]. In Fe-NCF-700–500, an N-doped carbon skeleton was obtained by defect engineering, providing potential catalytic activity for accelerating iodine conversion [35]. Especially, the Fe-NCF-700–500 with amorphous Fe_2N would provide possible anchor sites for the loading of stable iodine species.

Typically, the survey spectra confirm the existence of C, N, O, Fe (Fig. S6 in Supporting information). Fig. 2e shows that the core-level C 1s peak can be deconvoluted into three parts, corresponding to C–C/C=C (284.7 eV), C–N (285.7 eV) and C–O (286.8 eV) [36,37]. In Fig. 2f, the high-resolution XPS spectra of N 1s is fitted into five peaks at 398.2 (pyridinic N), 398.8 (Fe-N), 399.8 (pyrrolic N), 400.6 (graphitic N) and 403.3 eV (oxygenated-N) [38]. Nitrogen doping, especially graphite nitrogen, has the best catalytic activity towards iodine conversion [35]. The Fe-N located at 398.8 eV is attributed to the bonding of Fe with nitrogen atoms in Fe_2N decorated carbon fibers [39]. Fe-N is the most commonly reported active site, and the high Fe-N ratio (Table S2 in Supporting information) in the Fe-NCF-700–500 would help to stabilize iodine species and alleviate the shuttle effect. As shown in Table S1 (Supporting information), the content of nitrogen gradually decreased from 16.3 atom% to 3.3 atom% with the elevated pyrolysis temperature possibly due to the decomposition and reconstruction of nitrogen at a high temperature [40]. The total content of N in Fe-NCF-700–500 is higher than those of other two samples, and thus the additional heteroatom would introduce more defect sites and adjust the electronic structure of carbon host, which is in agreement with Raman spectra characterization.

The peak located at around 700 eV is related to Fe 2p core level [41]. The relatively higher content of Fe in Fe-NCF-700–500

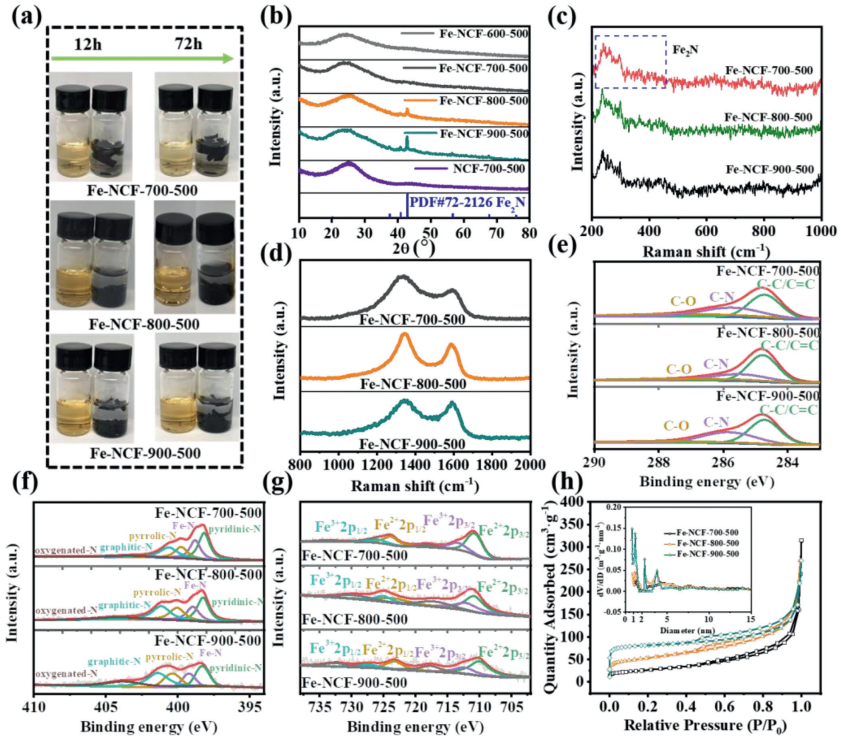

Fig. 2. (a) The iodine adsorption experiments. (b) XRD patterns of Fe-NCF under different temperatures N_2 calcination. (c, d) Raman spectra of Fe-NCF-T-500. (e) High-resolution XPS spectra of C 1s, (f) N 1s, (g) Fe 2p. (h) N_2 adsorption−desorption of Fe-NCF under different temperature and pore-size distribution curves.

is shown in Table S1. In addition to the satellite peak, the main peaks can be ascribed to Fe $2p_{1/2}$ and Fe $2p_{3/2}$ of Fe^{2+} and Fe^{3+} (Fig. 2g), suggesting the mixture of multi-valence Fe phrase and the existence of iron nitride. It has been reported Fe_2N as a typical interstitial compound does not conform to the simple valence rule and can be identified as a mixed valence state. Based on XPS analysis, it is clear that the Fe-N component in the amorphous Fe_2N decorated carbon fiber is an important factor to improve the redox reactions of iodine.

Then the effect of temperature on pore structure is compared in Fig. 2h. The N_2 adsorption/desorption curves exhibit micro- and meso–porous structures. According to the pore distribution curve, it corresponds to the type IV isotherm. The sample has higher surface area and wider pore size distribution with increasing temperature. Typically, the average pore size of Fe-NCF-T-500 is in the micro- and meso–pore size range. Such hierarchical porous structure would facilitate the redox conversion of iodine. Fe-NCF-700–500 does not have a maximum specific surface and pore volume, meaning that the ECSA is not the decisive factor affecting the performance. The key point to improve the performance of zinc-iodine battery is to stabilize the iodine and inhibit the shuttle of polyiodide.

To evaluate the electrochemical performance of the cathodes under different pyrolysis temperatures, cyclic voltammetry tests were carried out in Fig. 3. No obvious redox pair for Fe-NCF-700–500 with increasing scan rate (Fig. 3a) exhibits the pseudocapacitive process [42,43]. The polar compound Fe_2N are common pseudocapacitive materials, which have the combined electrochemical characteristics of double-layer capacitance and battery. To thoroughly investigate the mechanism of the reaction, the capacitance contribution with various scan rates is calculated according to Eq. 1:

$$i = k_1 v + k_2 v^{1/2} \quad (1)$$

The capacitive contribution ratio at 0.1, 0.2, 0.4, 0.6, 0.8 mV/s is gradually increased. Fig. 3c exhibits the capacitance contribution of Fe-NCF-700–500 and the good rate performance would be contributed to the fast kinetics of the redox reaction that is not limited by the semi-infinite diffusion [44,45]. In addition, at relatively small scan rates, the contributions of diffusion-controlled and capacitive behaviors are comparable. The electrochemical characteristics of pseudocapacitance can be described as (1) a linear or pseudo-linear relationship between voltage and state of charge (dQ/dV), (2) the near-ideal electrochemical reversibility, and (3) the surface-kinetic control. Increasing the calcination temperature, the obvious redox peaks are referred to the redox conversion of I_2/I^- with small peak potential shift in Fe-NCF-800–500 and Fe-NCF-900–500 (Figs. S8 and S9 in Supporting information). With the increase of temperature, the CV curves and corresponding charge-discharge curves show the obvious characteristics of Faraday reactions. For the Fe-NCF-800–500 and Fe-NCF-900–500 samples, the reaction characteristic is consistent with the typical Faradaic dominated reaction with the *quasi*-reversible process. As shown in Fig. 3b, Figs. S8b and S9b, CV curves under different cycles basically coincide due to the good reversibility. The ratio of capacitance contribution for three samples increase with the increase of scan rates. Compare to Fe-NCF-800–500, the different electrochemical behaviors of Fe-NCF-700–500 would be attributed the effect of pyrolysis temperatures.

To compare the performance differences of samples at different pyrolysis temperatures, the long cycling tests at different rates were carried out. The specific capacity of Fe-NCFs without active iodine is about 25 mAh/g (Fig. S10 in Supporting information). The initial capacity of Fe-NCF-700–500 is much higher than Fe-NCF-800–500 and Fe-NCF-900–500 at 2 C with the coulomb efficiency is 98% for the first cycle [46]. The batteries assembled by I_2/Fe-NCF-700–500 cathode exhibit the specific capacity of 214 mAh/g after 1500 cycles, and the capacity retention rate reaches 79%. In

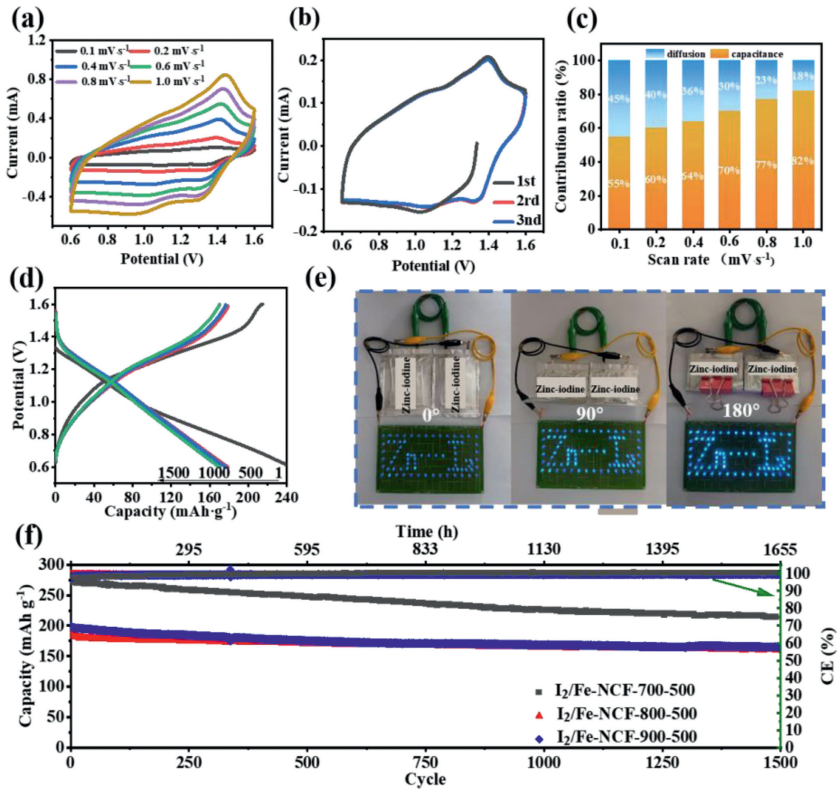

Fig. 3. (a) CV of Fe-NCF-700–500 with different scan rates, (b) under 0.2 mV/s with different cycles. (c) Capacitance contribution calculation. (d) Charge-discharge curves at various cycles of Fe-NCF-700–500. (e) Soft package battery test. (f) Long cycling performance at 2 C of Fe-NCF with various pyrolysis temperatures.

contrast, the I_2/Fe-NCF-800–500 and I_2/Fe-NCF-900–500 can maintain 160 and 165 mAh/g after 1500 cycles at 2 C, which is much lower than samples Fe-NCF-700–500. The long cycling test of I_2/Fe-NCF-600–500 (Fig. S11 in Supporting information) suggest the poor stability and low specific capacity due to the incomplete carbonization at low temperature. As shown in Fig. S12 (Supporting information), the specific surface area of the Fe-NCF-600–500 is very small and the pore structure is very few, which is not conducive to active iodine loading and redox reduction. For I_2/Fe-NCF-700–500, the amorphous structure would expose more reactive sites on the surface of Fe_2N, with the presence of nitrogen doping, thereby reducing the reaction polarization and significantly improving reaction kinetics. Besides, the zinc iodine batteries with an Fe-doped carbon fiber cathode were tested at 5 C and 10 C in Fig. S13 (Supporting information). As shown in the rate performance (Fig. S14 in Supporting information), the Fe-NCF-700–500 can almost recover to the original capacity, indicating the superior reversibility of the reaction. With good rate performance, the capacity of Fe-NCF-700–500 is higher than Fe-NCF-800–500 and Fe-NCF-900–500 both at 5 C and 10 C, can reach the capacity of 177 and 146 mAh/g, respectively. In Table S3 (Supporting information), the I_2/Fe-CF-700–500 composite cathode also demonstrated superior cycling stability compared with the reported zinc-iodine battery. It can be concluded that the hybrid composite of amorphous Fe_2N and carbon fiber can improve the charge transport ability and the binding ability of iodine species to promote the reversibility of the redox reaction. The Fe-NCF-700–500 were assembled into the soft pack battery, which, through bending test, could light up the small lamps even under 180°, and could sustain power supply over 50 h (Fig. 3e).

To identify the reaction process, *in-situ* Raman spectroscopy (Figs. 4a and b) exhibits the peaks for I_3^- and I_5^- at approximately 104 and 159 cm^{-1}, respectively. The adsorbed iodine would accept electrons from the carbon host, leading to the formation of I^- and subsequent polyiodide (I_3^- and I_5^-) [47]. The strong iodine species in the Fe-NCF-800–500 when compared with the Fe-NCF-700–500 sample, reflects the weak bonding effect on iodine species. Combined with the charge-discharge curve, I_3^- and I_5^- are presence in a slightly narrower potential window of around 1.0–1.60 V in the Fe-NCF-700–500 samples. Importantly, the wider peak potential range of iodine species indicates the slower conversion kinetics. In contrast, the narrower signal of iodine species in the Fe-NCF-700–500 sample shows the faster conversion between I_2 and I^-. The results show that the dispersion of iron nitride among porous carbon fibers has a catalytic effect on redox reaction of iodine species conversion. Combined with the capacitance contribution analysis above, the fast conversion reaction is carried out. The UV–vis spectra (Fig. 4c) were conducted to further confirm the faster conversion of iodine species in Fe-NCF-700–500. The weakest peak of I^- can be detected in Fe-NCF-700–500, and the relatively smooth fiber after cycling indicate that the presence of amorphous iron nitride would enhance the iodine adsorption on carbon fiber for improving the cycling performance. From the electrochemical impedance spectroscopy (Fig. 4d), the charge transfers resistance value of I_2/Fe-NCF-700–500 is smaller than those of I_2/Fe-NCF-800–500 and I_2/Fe-NCF-900–500. According to the formula, the smaller the charge transfer resistance, the lower the charge-transfer activation energy (E_a) at the same temperature, which indicates the faster kinetics of Fe-NCF-700–500 samples.

To figure out how to confine the iodine species, the interfacial interaction between host materials and iodine species was investigated by DFT calculation. From the Partial density of state (PDOS) pattern of I_2 molecule (Fig. 4e) in combination with the molecular orbitals, the unoccupied status of σ_p^* anti-bond orbital shows the discrete mode of separation [48]. In the presence of conductive substrates, the continuous pattern near the Fermi level shows the

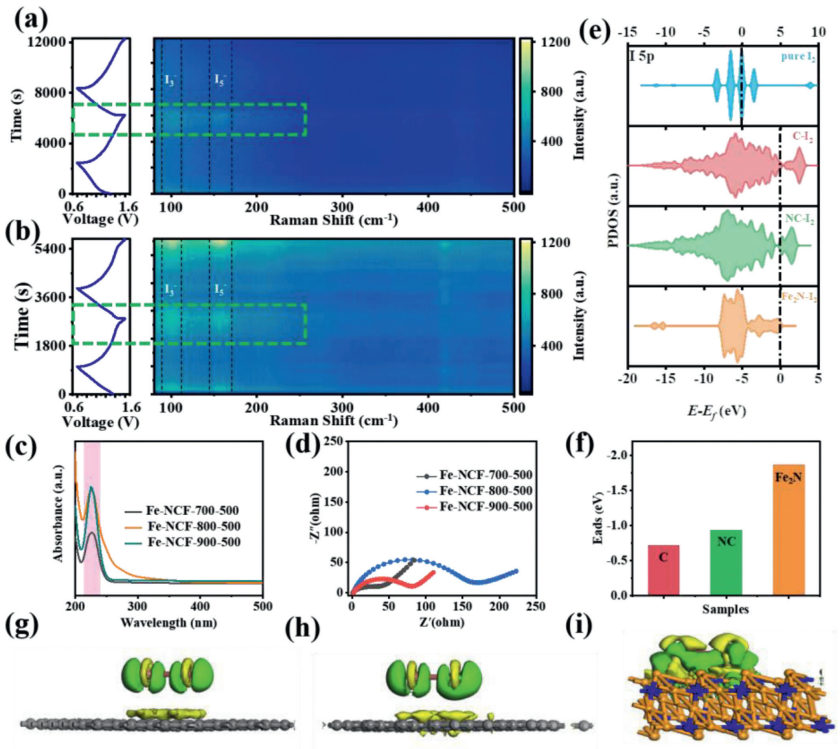

Fig. 4. *In-situ* Raman spectra of (a) Fe-NCF-700–500, (b) Fe-NCF-800–500 and corresponding discharge-charge curves. The dashed box marks the potential interval where polyiodide appears. (c) UV-vis test of Fe-NCF-T-500 after 50 cycles. (d) EIS spectra of Fe-NCF annealed under different temperatures. (e) PDOS for I_2 adsorption on different substrates. Calculations are based on (011) of Fe_2N. (f) The calculated adsorption energy of I_2 binding with C, NC and Fe_2N. Optimized charge density difference patterns of (g) C, (h) NC and (i) Fe_2N (011) for the binding of I_2. The cyan part means the charge accumulation, and the yellow part means the charge depletion. Gray, brown, yellowish brown and blue balls represent C, I, Fe and N atoms.

obvious electron transfer between iodine and the substrate. The interaction between substrate and iodide species was further simulated by the difference charge density patterns. The more negative adsorption energy indicates a stronger adsorption capacity [49]. According to Fig. 4f, the adsorption energy of pure carbon fiber for I_2 is −0.72 eV, which is the smallest than those of other substrates. Both nitrogen-doped carbon (NC) and Fe_2N nanoparticles have more negative adsorption energy for iodine molecule. The presence of iron nitride has a stronger binding force to iodine species, thus improving the cycling performance of zinc-iodine battery. Figs. 4g-i show the optimized charge density difference patterns of three hosts for the binding of I_2. Based on the above analysis, the hierarchical porous structure can be loaded with iodine and provide additional space for the reversible redox reaction. The interconnected 3D carbon skeleton facilitates the electrons transport for the rapid redox reactions. Furthermore, the well dispersed Fe_2N would enhance the electrocatalytic conversion of iodine, thus suppressing the shuttle effect. Therefore, such unique features contribute to the improved iodine conversion reaction for enhancing battery performance.

In summary, the iron nitride decorated N-doped carbon fibers (Fe-NCF) with abundant defect sites were prepared to enhance the electrical conductivity and porosity for loading iodine. With the porous and fibrous structure and favorable composition with iron nitride, the composited fiber electrode exhibited a large specific capacity of 214 mAh/g at 2 C with the capacity retention of around 100%. Even at a larger current density of 5 C, the electrode exhibited the discharging capacity of 177 mAh/g with the good cycling stability for 5000 cycles. The combination of experimental results and theoretical calculation provide fundamental explanation on the electrocatalytic conversion mechanism. With the promoted confinement effect of porous structure with nitrogen doping, the *in-situ* formation of the amorphous Fe_2N provide active sites for favorable anchoring iodine and subsequently accelerate the electrocatalytic conversion, thus mitigating the shuttle effect for the improved battery performance. This in-depth understanding inspires us to modify the porous carbon with metal nitride for improving the performance of rechargeable iodine-based batteries.

Declaration of competing interest

The authors declare that they have no known competing financial interests or personal relationships that could have appeared to influence the work reported in this paper.

Acknowledgments

This work was financially supported by the National Natural Science Foundation of China (No. 22175108), the Natural Scientific Foundation of Shandong Province (Nos. ZR2020JQ09 and ZR2022ZD27) and Taishan Scholars Program of Shandong Province, Project for Scientific Research Innovation Team of Young Scholar in Colleges, Universities of Shandong Province (No. 2019KJC025). The authors also acknowledge the assistance of the Analytical Center for Structural Constituent and Physical Property of Core Facilities Sharing Platform, Shandong University.

Supplementary materials

Supplementary material associated with this article can be found, in the online version, at doi:10.1016/j.cclet.2023.108232.

References

[1] Y. Miao, Y. Zheng, F. Tao, et al., Chin. Chem. Lett. 34 (2023) 107121.
[2] E. Pomerantseva, F. Bonaccorso, X. Feng, et al., Science 366 (2019) 6468.

[3] S. Yang, X. Guo, H. Lv, et al., ACS Nano 16 (2022) 13554–13572.
[4] D. Lin, Y. Li, Adv. Mater. 34 (2022) 2108856.
[5] Q. Zhao, Y. Lu, Z. Zhu, et al., Nano Lett. 15 (2015) 5982–5987.
[6] Z. Meng, X. Tan, S. Zhang, et al., Chem. Commun. 54 (2018) 12337–12340.
[7] Z. Meng, H. Tian, S. Zhang, et al., ACS Appl. Mater. Interfaces 10 (2018) 17933–17941.
[8] Z. Su, H.Y. Ling, M. Li, et al., Carbon Energy 2 (2020) 265–275.
[9] D. Gong, B. Wang, J. Zhu, et al., Adv. Energy Mater. 7 (2017) 1601885.
[10] L. Yan, S. Zhang, Q. Kang, et al., Energy Stor. Mater. 54 (2023) 339–365.
[11] H. Tian, S. Zhang, Z. Meng, et al., ACS Energy Lett. 2 (2017) 1170–1176.
[12] M. Han, J. Yao, J. Huang, et al., Chin. Chem. Lett. 34 (2023) 107493.
[13] Y. Chai, X. Xie, Z. He, et al., Chem. Sci. 13 (2022) 11656–11665.
[14] J. Ma, M. Liu, Y. He, et al., Angew. Chem. Int. Ed. 60 (2021) 12636–12647.
[15] Y. He, M. Liu, J. Zhang, Adv. Sustain. Syst. 4 (2020) 2000138.
[16] H.Y. Shi, Y.J. Ye, K. Liu, et al., Angew. Chem. Int. Ed. 57 (2018) 16359–16363.
[17] B. Li, J. Liu, Z. Nie, et al., Nano Lett. 16 (2016) 4335–4340.
[18] F. Wang, Z. Liu, C. Yang, et al., Adv. Mater. 32 (2020) e1905361.
[19] L. Ma, Y. Ying, S. Chen, et al., Angew. Chem. Int. Ed. 60 (2021) 3791–3798.
[20] Q. Chen, S. Chen, L. Zhao, et al., Chem. Eng. J. 431 (2022) 133961.
[21] C. Prehal, H. Fitzek, G. Kothleitner, et al., Nat. Commun. 11 (2020) 4838.
[22] H. Pan, B. Li, D. Mei, et al., ACS Energy Lett. 2 (2017) 2674–2680.
[23] C. Sun, X. Shi, Y. Zhang, et al., ACS Nano 14 (2020) 1176–1184.
[24] X. Li, N. Li, Z. Huang, et al., Adv. Mater. 33 (2021) 2006897.
[25] H.X. Dang, A.J. Sellathurai, D.P.J. Barz, Energy Stor. Mater. 55 (2023) 680–690.
[26] D. Lin, D. Rao, S. Chiovoloni, et al., Nano Lett. 21 (2021) 4129–4135.
[27] W. Liu, P. Liu, Y. Lyu, et al., ACS Appl. Mater. Interfaces 14 (2022) 8955–8962.
[28] L. Han, H. Huang, J. Li, et al., J. Mater. Chem. A 7 (2019) 24400–24407.
[29] J. Liu, Q. Jia, J. Long, et al., Appl. Catal. B 222 (2018) 35–43.
[30] M. Liu, Q. Chen, X. Cao, et al., J. Am. Chem. Soc. 144 (2022) 21683–21691.
[31] J. Xiao, Y. Xu, Y. Xia, et al., Nano Energy 24 (2016) 121–129.
[32] Y. Lou, J. Liu, M. Liu, et al., ACS Catal. 10 (2020) 2443–2451.
[33] Y. Tian, X. Liu, L. Xu, et al., Adv. Funct. Mater. 31 (2021) 2101239.
[34] Y. Tong, Y. Wu, Z. Liu, et al., Chin. Chem. Lett. 34 (2023) 107443.
[35] T. Liu, H. Wang, C. Lei, et al., Energy Stor. Mater. 53 (2022) 544–551.
[36] H. Lei, Z. Wang, F. Yang, et al., Nano Energy 68 (2020) 104293.
[37] D. Yu, A. Kumar, T.A. Nguyen, et al., ACS Sustain. Chem. Eng. 8 (2020) 13769–13776.
[38] M. Wang, W. Yang, H. Wang, et al., ACS Catal. 4 (2014) 3928–3936.
[39] Z. Chen, Y. Li, L. Lei, et al., Catal. Sci. Technol. 7 (2017) 5670–5676.
[40] Y. Du, T. Liu, B. Yu, et al., Mater. Chem. Phys. 135 (2012) 884–891.
[41] L. Yang, S. Feng, G. Xu, et al., ACS Sustain. Chem. Eng. 7 (2019) 5462–5475.
[42] Z. Su, C. Tong, D. He, et al., J. Mater. Chem. A 4 (2016) 8541–8547.
[43] L. Wang, X. Li, J. Ma, et al., Sustain. Energy 2 (2014) 39–43.
[44] X. Li, M. Li, Z. Huang, et al., Energy Environ. Sci. 14 (2021) 407–413.
[45] C. Choi, D.S. Ashby, D.M. Butts, et al., Nat. Rev. Mater. 5 (2019) 5–19.
[46] S. Fleischmann, J.B. Mitchell, R. Wang, et al., Chem. Rev. 120 (2020) 6738–6782.
[47] N. Jung, C.C. Andrew, N. Kim, et al., ACS Nano 4 (2010) 7005–7013.
[48] Z. Su, Z. Wei, C. Lai, et al., J. Ma, Energy Stor. Mater. 14 (2018) 129–135.
[49] W. Sun, C. Liu, Y. Li, et al., ACS Nano 13 (2019) 12137–12147.